sciendo

POLISH MARITIME RESEARCH 3 (111) 2021 Vol. 28; pp. 61-75
10.2478/pomr-2021-0034

FLUID–STRUCTURE INTERACTION VIBRATION EXPERIMENTS AND NUMERICAL VERIFICATION OF A REAL MARINE PROPELLER

Benqiang Lou [1]
Hongyu Cui *[2]
[1] School of Naval Architecture and Ocean Engineering, Jiangsu University of Science and Technology, China
[2],* State Key Laboratory of Structural Analysis for Industrial Equipment, School of Naval Architecture Engineering, Dalian University of Technology, China
* Corresponding author: *cuihongyu@dlut.edu.cn (H. Cui)*

ABSTRACT

The design of lifting blade shapes is a key engineering application, especially in domains such as those of marine propellers, hydrofoils, and tidal energy converters. In particular, the excitation frequency must be different from that of the structure to avoid resonance. The natural frequency in the cases where the fluid–structure interaction (FSI) is considerably different if considering the coupling added mass (AM) of the water. In this study, vibration experiments were performed using a real propeller in air and water. The modal parameters, natural frequencies, and mode shapes were determined. Validations were performed using 3D solid and acoustic elements in a direct coupling finite element format. The modal results and AM ratios were in agreement with the experimental results. Convenient application and high efficiency are basic requirements for an engineering application. Therefore, an empirical formula was established for the first-order FSI natural frequency to enable rapid estimation, thereby satisfying this requirement.

Keywords: Fluid–structure interaction, Real propeller vibration experiments, Direct coupling, Finite element method, Added mass ratios.

INTRODUCTION

As a key component of ship propulsion systems, the propeller represents a valuable technological advancement to supply the propulsion power. When a propeller rotates, it acts as a reactive thruster and pushes a mass of fluid astern. Several key technical aspects of propellers have been described by Carlton [1], pertaining to energy-saving, propulsion, centrifugal force and hydrodynamic force, cavitation, and noise and vibrations, among others. Recently, Król [2] reviewed the topics of rotor–stator propulsor system design and operation, described the current state of the art and summarised various researchers' results from installing energy-saving devices. The analysis has proved very useful, giving the expected trend of a higher efficiency gain due to the ESD installation for a higher propeller loading. Our present work is focused on the fluid–structure interaction (FSI) vibrations of an actual propeller obtained from an inland river ship, with emphasis on the modal parameters and reduction coefficients of the frequencies.

When the excitation frequency coincides with the natural frequency of the structure, the structure may exhibit a high level of vibrations that may lead to structural fatigue and failure. When a propeller immersed in a fluid oscillates, the surrounding fluid may cause the natural frequencies to be lower than those in air. The current propeller design is improving with novel designs that are different from the conventional processes. Therefore, we consider whether assigning a reasonable approximation can avoid the vibration resonance of the blade in a water medium, particularly in the initial design stage.

Academics have attempted to examine the FSI through experimental, theoretical, and numerical simulation approaches. For instance, the original tests were performed during World War II [3], considering approximately 50 models of the 3-bladed KCA series and several models of the KCC and KCD series. The most extensive data correspond to a collection of propeller models that were tested at King's College 60 years ago [4]. Parsons et al. [5] used the 3D lifting line method coupled with the 2D unsteady thin foil theory to examine four-blade Wageningen B-Series propellers vibrating because of unit heave or unit pitch oscillations. Hyloarides and Van Gent [6] tested B-series propellers using the lifting surface method. Zhao et al. have performed independent studies in the field of FSI vibration analysis since the 1990s ([7], [8], [9]), with their contributions covering the theory, experiments, and numerical algorithms.

The concept of the added mass (AM) was generalised by Korotkin [10], and this aspect was considered to reduce the frequencies of free oscillations. Eq. (1) was used to determine the added mass coefficients analytically, with reference to the fluid density and total kinetic energy outside of the surface. Thereafter, Ghassemi and Yari [11] applied Eq. (1) to numerically examine the FSI sphere, ellipsoid, and propeller. However, the derived AM coefficient matrix corresponded only to the first-order natural frequencies.

$$\lambda_{ik} = -\rho \iint \frac{\partial \varphi_i}{\partial n} \varphi_k \, dS \tag{1}$$

More advanced equipment has been used to measure underwater propeller vibration, such as the laser Doppler vibrometer (LDV), scanning LDV, and tracking LDV. Castellini and Santolini [12] performed LDV testing on a naval propeller rotating underwater and compared the time histories of various rotational speeds during operation in water and air. Abbas et al. [13] obtained LDV measurements to perform an underwater propeller vibration analysis. Guangnian [14] used particle image velocimetry technology to study the characteristics of the tip flow field of a DTMB-P4119 propeller in a large cavitation tunnel.

Numerical analyses and experiments are often conducted in a synchronous manner. For instance, as described by Vaz et al. [15], several institutions have used eight different codes, specifically, ANSYS CFX®, ANSYS Fluent®, Excalibur, FINETM/Marine, OpenFOAM, PROCAL, ReFRESCO, and Star CCM+®, to simulate the propeller cavitation dynamics. Computations for the DTMB-P4119 model were carried out by Nouroozi and Zeraatgar [16] in symmetric flow using FLUENT, and validated by the available experimental data. Nadery and Ghassemi [17] used STAR-CCM+ to calculate the hydrodynamic coefficients of the propeller NACA0006, and discussed the propeller in oscillating flows with and without a stator. Zhang et al. [18] applied RANS onto geometrically similar propellers in cavitation predication, and discussed the influences of the mesh density and time steps. A meaningful numerical solution may be achieved by combining the error estimates in simulations with the uncertainty quantification realised in the experiments. Furthermore, when experimental data are not available, numerical simulations may be a worthy alternative choice.

The simulation of FSI is a highly specific topic in computational mechanics, as reported by Sigrist [19], and can provide a general framework to classify various coupling phenomena. For this FSI vibration problem, two approaches can be recognised in the numerical simulation, as shown in Fig. 1: the direct method (using fluid–structure coupling codes) and the indirect method (coupling fluid and structure codes).

The governing equations of FSI are formulated as a unique coupled system in the direct method. The structural deflections of the propeller and resulting hydrodynamic forces lead to

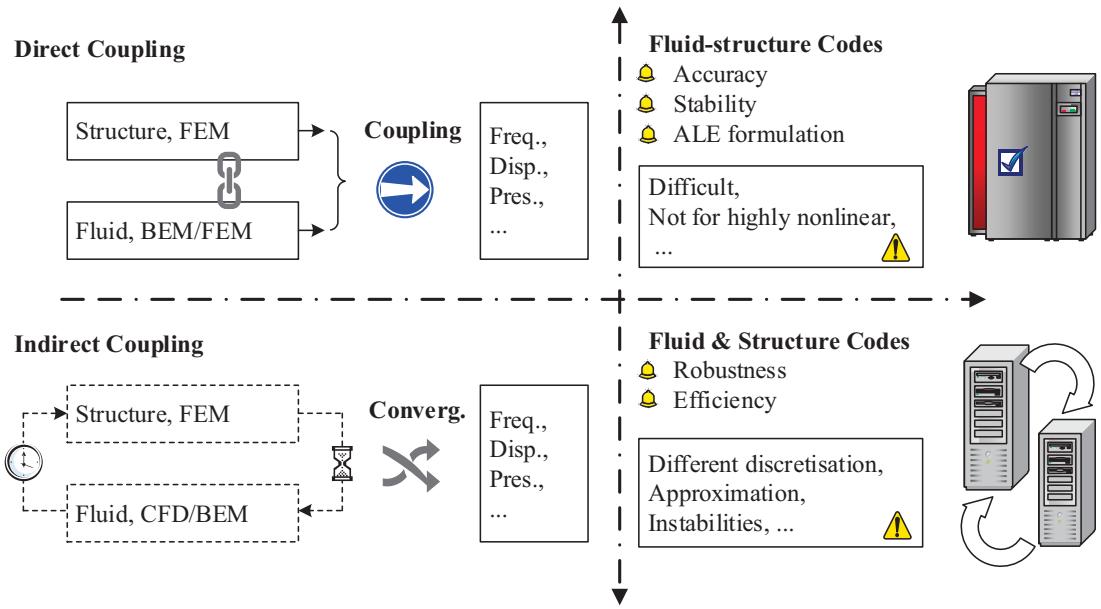

Fig. 1. Numerical simulation: coupled fluid–structure and fluid and structure code coupling [19]

changes in the structural response, which are described as a set of coupled equations. Suo and Guo [20] applied the 3D hydroelasticity theory for propeller vibrations in water and incorporated the findings into finite element codes to determine the natural frequencies. Lin and Lin [21] performed the hydroelastic analysis of propellers based on a coupled 3D non-linear FEM and non-cavitating lifting surface method. In general, the finite element (FEM) and boundary element (BEM) methods can be combined as a promising numerical technique to address vibro-acoustic coupling. Zou et al. [22] extended the coupled FEM/BEM, taking into account the effect of the shaft. Li et al. [23] investigated the effects of the excitation frequency and inflow velocity on the added mass and damping of elastic marine propellers, by using the coupled FEM/BEM method.

In the indirect method, the simulations are primarily based on an iterative procedure. The governing equations of the fluids and structures are solved separately. Coupling helps realise the exchanges between two codes. The hydrodynamic forces are computed and added onto the blade surface, and are subsequently affected by the structural responses. The iterative procedures are implemented for the fluid pressures and structural responses sequentially until convergence. Using ABAQUS®, Young [24], [25] examined flexible composite propellers with large deformations and determined the hydroelastic pressure by using the BEM algorithm. Subsequently, the iterations were implemented until convergence was attained between the BEM and FEM solvers. He et al. [26] developed a 3D FEM/computational fluid dynamics (CFD) coupling algorithm to investigate the natural frequencies, mode shapes, and hydrodynamic load coefficients of a highly skewed propeller. Lee et al. [27] introduced a BEM-FEM (ABAQUS)-based algorithm to predict the unsteady thrust and torque coefficients for flexible propellers. Neugebauer et al. [28] analysed the FSI of propellers by using a CFD-based method. Kapuria and Das [29] analysed and optimised the hydrodynamic performance of a composite propeller through FEM/CFD coupling.

Several basic mode shapes are illustrated in Fig. 2. The existing reports [1] indicated that the vibration modes are usually dominated by whipping and torsion, and no lateral deformation occurs. In this scenario, the structure exhibits a strong anti-lateral inertia, and the fundamental mode corresponds to the first-order whipping case.

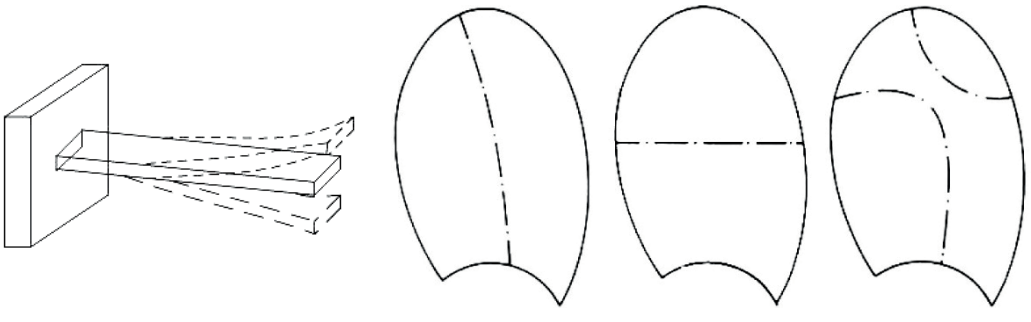

Fig. 2. FSI propeller blade modes [1]

The FSI phenomenon is not only of academic interest, but also has practical significance. For instance, in the case of emerging marine propellers, there are few numerical codes in wide use and many aspects have not been sufficiently clarified. The change in the natural frequency in different media (air and water) is of particular significance. It is unclear whether the frequency reduction can be considered as a set of numbers characterising the intensity of the coupling or if certain laws exist for simple applications, as reported by MacPherson et al. [30] in a semi-empirical fashion.

In contrast to these studies, in the present work, an actual propeller was considered. In particular, experiments provide meaningful practical data for physical insight and code verification. Three main categories of FSI research challenges were considered in this work. In the theoretical context, the mathematical formulation of the coupling was established in a unique finite element format. A transfer function was used to define the impulse response relationship of a physical system, and this frequency response function (FRF) was explained to enhance the basis of the experiments. The measurements conducted in the experiment helped define the device characteristics and system settings. The natural frequencies and mode shapes of a real propeller were identified through impact hammer testing. The physics of FSI oscillation coupling effects has been fully understood by the existing software tool, which can corroborate the experimental results. Finally, an empirical qualitative expression was presented for the FSI first-order natural frequency estimation. By using this formula, an engineer can predict the FSI vibration. The expression can probably be used to promptly determine whether the excitation frequency has fallen into the resonance frequencies or not, during the concept design stage.

FOUNDATION AND ALGORITHM OF FSI

PHYSICAL MODEL AND ASSUMPTIONS

The FSI is recognised as an inter-field relationship, the basic mechanism of which can be described as follows: the flow may induce a fluctuation in the pressure and/or deformation and velocity of the structure. Moreover, the structural motion may change the flow condition at the interface with the fluid. The fluid momentum (Navier–Stokes) and continuity equations can be simplified to obtain the convective wave equation by considering the following assumptions:

(1) The fluid is compressible and irrotational, and the pressure disturbance of the fluid is small.

(2) No body force or viscous stresses exist.
(3) The components of the hydrodynamic forces and inertial torques act on a propeller placed arbitrarily in an immovable fluid.
(4) The propeller is immersed sufficiently deep in water; thus, the influence of the water surface can be excluded.

In the existing studies, two code combinations (such as the FVM-FEM, BEM-FEM, and SPH-FEM) have often been used to examine the FSI. However, when considering the convenience of mesh grids, seamless transformation of the physical information on the interface, and availability of commercial code resources, the FEM may be the most suitable choice. Accepting a unique coupling grid introduces smaller errors, and the transformation may be sufficiently accurate. The FEM can be used to compute the pressure and velocity fields at arbitrary interior/exterior points. The following section describes the mathematical algorithm. For conciseness, only the key equations and matrices are presented.

GENERAL FEM ALGORITHM FOR THE FSI COUPLING SYSTEM

The motion of an ideal compressible fluid can be described as a wave equation. If the density indicates the balance of the mass flow entering and leaving, and an infinitesimal control volume equals the rate of the change in the density, the mass conservation can be described as in Eq. (2).

$$\frac{\partial \rho}{\partial t} + \rho_0 \cdot \nabla v_i = 0, \text{ where } i = 1, 2, 3 \tag{2}$$

The governing equation of the momentum conservation can be expressed as in Eq. (3).

$$\rho_0 \cdot \frac{\partial v_i}{\partial t} = -\nabla p \tag{3}$$

We assume a small compressibility, taking into account that the density changes owing to the elastic deformability related to the pressure changes, and obtain the following state equation:

$$dp = c_0^2 \cdot d\rho \tag{4}$$

where
ρ is the density of the fluid;
v_i is the curl of the perturbation velocity;
p and p denote the density and pressure;
c_0 is the sound velocity in the fluid, assuming a constant entropy.

By substituting Eqs. (3) and (4), the governing equation can be obtained. Consequently, Eq. (2) can be rewritten in a general form as Eq. (5):

$$\nabla^2 p - \frac{1}{c_0^2} \cdot \frac{\partial^2 p}{\partial t^2} = 0 \tag{5}$$

where

$$\nabla^2 = \frac{\partial^2}{\partial x^2} + \frac{\partial^2}{\partial y^2} + \frac{\partial^2}{\partial z^2} \tag{6}$$

and $\boldsymbol{p}$ is the potential of the fluid pressures, owing to which the potential flow problem satisfies the superposition principle.

Typically, in stationary solid conditions, both the normal and tangential velocities reduce to zero. The fluid viscosity is neglected; and the no-slip boundary condition cannot be enforced on a structure–fluid boundary. Therefore, as the boundary limit, the normal component of the velocity is continuous, as indicated in Eq. (7), and the pressures and stresses are continuous on the surface, as indicated in Eq. (8).

$$\frac{\partial p}{\partial n_\mathrm{f}} + \rho_0 \frac{\partial^2 v}{\partial t^2} \cdot n_\mathrm{f} = 0 \tag{7}$$

$$\sigma \cdot \overrightarrow{n_\mathrm{S}} = p \cdot \overrightarrow{n_\mathrm{f}} \tag{8}$$

The boundary conditions must be specified on the surfaces and infinity. Therefore, the wave equation of Eq. (5) is supplemented as follows:

(1) Impenetrability of the infinite boundary condition.

$$\frac{\partial p}{\partial n_\mathrm{f}} = 0 \tag{9}$$

(2) Free surface condition: The disturbance caused by the body moving through a fluid that is initially at rest decays to zero. This condition is also known as the Sommerfeld boundary condition [31].

$$\frac{\partial p_{(t)}}{\partial z} + \frac{c_0^2}{g} \cdot \frac{\partial^2 p}{\partial t^2} = 0 \tag{10}$$

The theorem of the 'variational principle' can be used to match the conditions of the geometry relation and continuous boundary conditions of the normal velocity and stress. According to the Galerkin principle, an identical form can be generated to that obtained by minimising the variational principle. Therefore, there exists a weak form in Eq. (11), in which the stabilising terms are integrated by parts, along with the boundary integral. In other words, for equilibrium to be ensured, the total potential energy must be zero for variants of the admissible displacement.

$$\iiint \left[\delta \nabla p \cdot \nabla p + \frac{1}{c_0^2}\frac{\partial^2 p}{\partial t^2}\right] dV + \iint \delta p \left(\frac{1}{g}\frac{\partial^2 p}{\partial t^2}\right) dS_\mathrm{f} + \iint \delta u (\rho_0 \frac{\partial^2 u}{\partial t^2} \cdot n_\mathrm{f})\, dS_0 = 0 \tag{11}$$

The weighted integral formulation of the structure can be expressed as in Eq. (12) [32]:

$$\iint \rho_s \frac{\partial^2 u}{\partial t^2} dS_f + \iint \sigma(u)\varepsilon(\delta u)\, dS_f - \iint \delta u(p \cdot n_f)\, dS_0 = 0 \tag{12}$$

The integral equations are simply statements of this variation with respect to certain variables. The variational principle specifies a scalar quantity such as $\boldsymbol{p}$ (pressure). Subsequently, the displacement can be approximated using the differential operators.

$$\begin{aligned} p(x,y,z,t) &\approx \sum N_i(x,y,z)\, p_i(t) = \boldsymbol{N}\boldsymbol{p}^e \\ u(x,y,z,t) &\approx \sum \bar{N}_i(x,y,z)\, u_i(t) = \bar{\boldsymbol{N}}\boldsymbol{u}^e \end{aligned} \tag{13}$$

where $\boldsymbol{N}$ and $\bar{\boldsymbol{N}}$ denote the shape functions of the pressure and displacement, respectively; $\boldsymbol{p}$ denotes a set of pressures of the fluid; and $\boldsymbol{u}$ denotes the displacement at the structural node.

We substitute the approximation presented in Eq. (13) into Eq. (11) and differentiate with respect to the stationary equilibrium. The approximation allows the use of the integral forms obtained elementwise and final form generation. Therefore, the FSI structure vibrations can be represented as a hypothetical set of displacement and pressure variables ($\boldsymbol{u}$, $\boldsymbol{p}$) in Eq. (14), for an undamped system [33], [34].

$$\begin{bmatrix} M_s & 0 \\ -Q^T & M_f \end{bmatrix} \begin{Bmatrix} \ddot{u} \\ \ddot{p} \end{Bmatrix} + \begin{bmatrix} K_s & \frac{1}{\rho_0} Q \\ 0 & K_f \end{bmatrix} \begin{Bmatrix} u \\ p \end{Bmatrix} = \begin{Bmatrix} F_s \\ 0 \end{Bmatrix} \tag{14}$$

where $\boldsymbol{Q}$ is the FSI matrix, with the element matrix being $Q^e = \iint \rho_0 N^T N dS$; $\boldsymbol{M}_f$ and $\boldsymbol{K}_f$ denote the mass and stiffness matrices of the fluid, with their element matrices $M_f^e = \iiint \frac{1}{c_0^2} N^T N\, dV + \iint \frac{1}{g} N^T N dS$ and $K_f^e = \iiint \frac{\partial N^T}{\partial x} \frac{\partial N}{\partial x} dV$, respectively; and $\boldsymbol{M}_s$ and $\boldsymbol{K}_s$ denote the mass and stiffness matrices of the structure, with $M_s^e = \iiint \rho_S \overline{N^T} \bar{N}\, dV$ and $K_s^e = \iiint B^T D B\, dV$, respectively.

The equation of motion for free vibration leads to the solution of the natural modes, for which the right side of the coupling functions is zero. Thus, Eq. (14) can be converted to Eq. (15).

$$\omega^2 \begin{bmatrix} M_s & 0 \\ -Q^T & M_f \end{bmatrix} \begin{Bmatrix} u \\ p \end{Bmatrix} = \begin{bmatrix} K_s & \frac{1}{\rho_0} Q \\ 0 & K_f \end{bmatrix} \begin{Bmatrix} u \\ p \end{Bmatrix} \tag{15}$$

The mass and stiffness matrices in an FSI system are asymmetrical and full, respectively: The stiffness matrix remains sparse with a limited bandwidth, whereas the mass matrix is densely populated. In general, Eq. (15) can be made symmetrical by using the subspace method or Lanczos iterative approaches, as described in handbooks [32], [33]. The coupled dynamic equation can be converted into a generalised eigen solution of Eq. (16).

$$[M'][\Psi][\Lambda] = [K_s][\Psi] \tag{16}$$

where $[\Psi]$is the eigen-vector matrix, that is, the mode shape, $[\Psi] = [\{\psi_1\}, \{\psi_2\} \cdots \{\psi_n\}]$, and $[\Lambda]$ represents the eigenvalues, that is, the natural frequencies.

From the theoretical standpoint [33], the condensed ($\boldsymbol{u}$, $\boldsymbol{p}$) formulation can describe the physical nature of the vibro-acoustic coupling. After solving this formulation, the hydro pressure and induced structural deformation owing to the pressure can be obtained in one step. Moreover, a computer program employing the same

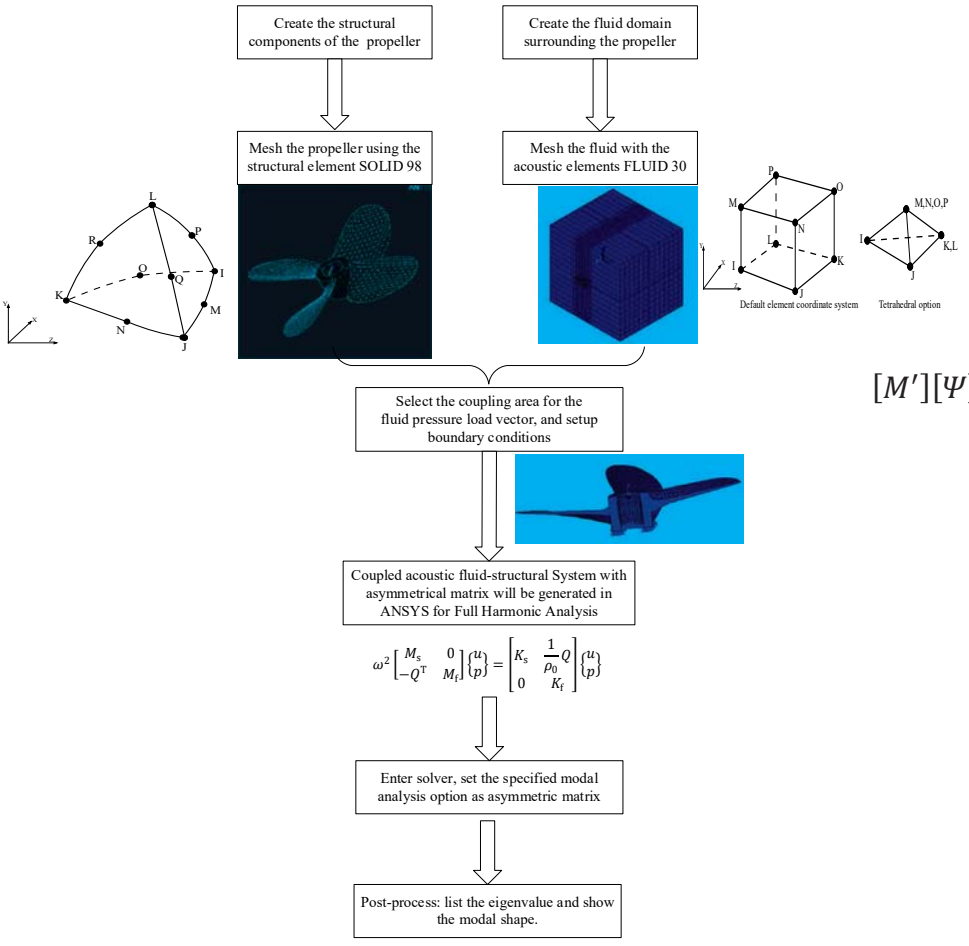

Fig. 3. Flowchart of the structure-fluid coupling analyses in ANSYS

standard operations can enable an evaluation of the quantities analogous to the calculations.

ALGORITHM OF THE ACCELERATION FRF

The FRF reflects the data transforms between the input excitation and output response in the frequency domain. The FRF is composed of the sum of motions of all the modes of vibration that have been excited, as the system is assumed to behave in a linear manner. A 'perfect' impact has an infinitely short duration, resulting in a rich spectrum. The 'impulse' input is considered commonly as a δ function, as indicated in Eq. (17).

$$\delta(t-\tau) = \begin{cases} \infty, & t = \tau \\ 0, & t = 0 \end{cases}$$
$$\int_{-\infty}^{\infty} \delta(t-\tau)dt = 1 \tag{17}$$

The duration is directly linked to the frequency content of the force excited. The transfer operation is defined as the Fourier transform of the time-domain differential equation to the equivalent frequency domain algebraic equations. The input function $f(t)$ satisfies the Dirichlet condition, and thus $F(\omega)$ can be computed using Eq. (18).

$$F(\omega) = \int_{-\infty}^{\infty} \frac{1}{2\pi} f(t) e^{-i\omega t} dt \tag{18}$$

The transform matrix is defined as $[H(\omega)]_{\ddot{x}}$ in Eq. (19), representing the appropriate FRF between a unit force and the response acceleration.

$$[H(\omega)]_{\ddot{x}} = \frac{\{\ddot{X}(\omega)\}}{\{F(\omega)\}} \tag{19}$$

where $\{\ddot{X}(\omega)\}$ is the acceleration response and $\{F(\omega)\}$ is the excited force.

The frequency domain parameter estimation uses data directly in the frequency domain. The impulse response function can match the multi-DOF free vibration physically.

$$[H(\omega)]_{\ddot{x}} = \sum_{i=1}^{N} \frac{1}{K_i} \frac{\omega^2 \{\psi_i\}\{\psi_i\}^T}{1-(\omega/\omega_i)^2} \tag{20}$$

The weighting, often known as the modal participation factor, is a function of the excitation and mode shape coefficients at the input and output degrees of freedom.

$$[H(\omega)]_{\ddot{x}} = \sum_{i=1}^{N} \frac{1}{K_i} \frac{\omega^2 A_i^r A_i^l}{1-(\omega/\omega_i)^2} \tag{21}$$

where ψ_i (and ψ_j) denote the normalised phase associated with the order of the points, which is the i^{th} mode; ω and ω_i are the circular frequencies; K_i is the generalised stiffness matrix; and A_i^r and A_i^l denote the amplitude of the phase shift $\{\psi_i\}$ at the point r and l, respectively.

In this manner, a large amount of modal information is contained in the transfer function, and it can be used to realise the mode recognition. This aspect is the principle of the 'impact hammer test' for the resonances.

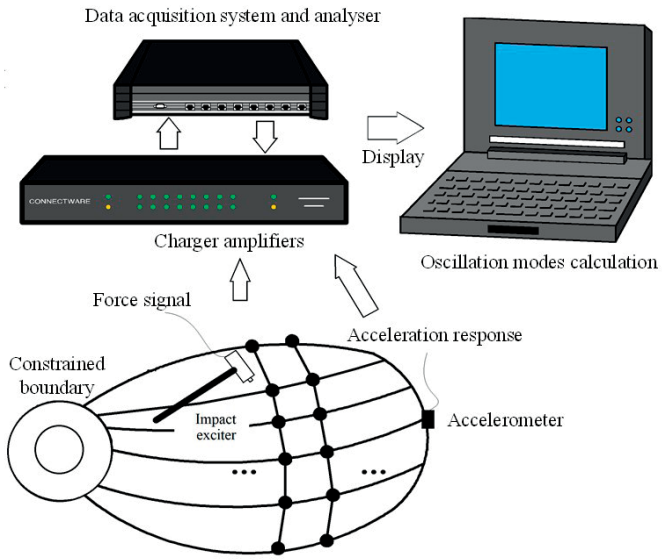

Fig. 4. Mechanical system for the modal testing of a real propeller

MODAL TESTING OF THE PROPELLER

Successful testing depends on several factors, and the hardware and equipment represent a key aspect, pertaining to the operator's communication link to the analyser. Fig. 4 shows a schematic of the construction of our test system. The approximate natural frequencies and a rough estimate of the corresponding mode shapes were first determined by measuring a series of FRFs. A multi-input and single-output approach was used. If ***n*** points are struck, the normalisation is based on the i^{th} largest point through the transfer functions, and the normalised results are connected in the order of the points, corresponding to the i^{th} mode. In the approach, a frequency domain model of the structure was used in conjunction with the FRF measurements.

To implement suitable rectifications, the following steps were performed: the first step involved signal generation. After the shaker trigger was armed, the force by the impact was recorded by the acceleration sensor. The analyser was initialised, and it acquired the signal once the force

transducer operated. The acceleration response corresponded to the externally mounted stores, when the accelerometer measurements at a single point within the store were available. The output voltage, external electric load resistance, and excitation frequency were measured and recorded.

The second step involved data acquisition and signal processing operations. The signal source supplied for signal conditioning was an alternating current voltage, converted from the mechanical vibration energy. The signal amplifiers converted the outputs to analogue voltages. The end of the charger amplifier was connected to a data acquisition equipment. The Data Auto Sample and Process System (DASP) software was used to perform the signal analysis and data acquisition at the interpolated points. Finally, the modal parameter identification was performed. The measurement functions for the averages and the frequency response analysis or spectrum analysis were realised using the analyser. In general, the DASP software includes the built-in FFT codes to determine the natural frequencies and display the mode shapes, and it can calculate the corresponding least squares error.

To implement these advanced experiments, state-of-the-art testing technologies were required, along with expensive equipment. The cost of these aspects can easily be justified because the impact hammer test is the most cost-efficient and effective experimental approach.

PROPELLER SPECIMEN

It is more meaningful to use a real propeller, because not only can the practical appearance help discover the physical phenomena, it can also provide a reference for the virtual digital world. The propeller geometry and material characteristics are listed in Table 1.

Tab. 1. Propeller data

Propeller type	MAU 4-40	
Number of blades	4	
Material	Ni-Al-Bronze Cu-3	
Weight	77.30	kg
Propeller diameter, D	0.562	m
Hub diameter, Φ	0.11	m
Hub depth, h	113.0	mm
Diameter of hub hole, r	30.0	mm
Propeller pitch ratio	0.688	
Expanded area ratio (EAR)	0.54	
Skew angle	10°	

A symmetrical structure was employed to simplify the test, as the modes would also be symmetric. As shown in Fig. 5, a quartered propeller was selected and labelled. The testing propeller is a real propeller obtained from an inland river ship, which can ensure authentic measurements. Moreover, it was challenging to access certain locations and determine the thickness of the blade. Therefore, it was necessary to scratch the grids and perform factory laser equipment measurements during the test preparation, which was expensive and tedious. The measured points corresponded to the intersections of the grid to be input into ANSYS® to provide an accurate representation of the propeller shape.

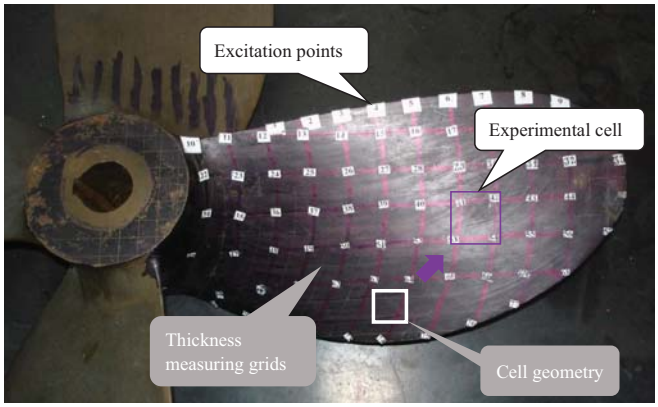

Fig. 5. Distribution and labelling of the test points on the propeller blade

INPUT AND SIGNAL COLLECTION EQUIPMENT

In general, a shaker is used to trigger the propeller with broadband random noise. Triggering can be performed for automatic re-arming after each trigger to ensure that several hammer impacts can be realised sequentially and averaged without the need to interact with the signal analyser. A hammer, MSC-1, was used to excite an impulse signal, and its details are presented in Table 2. The shaker generated a voltage signal proportional to the exciting force. A transducer was fixed at the end of the shaker. The shaker amplifier gain was linearly proportional to the excitation acceleration amplitude.

Impact tips with different hardness values were selected to be used with the hammer for the considered measurement frequency range. When low frequency measurements were required, a soft rubber tip was used, and when high frequency measurements were required, a hard metal tip was used.

Tab. 2. Technical specifications and details of the hammer

Type	MSC – 1
Force measurement, (N)	0–500
Sensitivity, (mV/N)	10.0
Resonant frequency, (Hz)	20 k
Impedance, (Ω)	< 100
Dimensions of hammer, (mm)	18 × 40
Weight, (g)	50

The accelerometer was the proximal signal gain equipment, which measured and recorded the accelerations. After the trigger was armed, the accelerometer waited for the impact to occur and started acquiring the signal data. The entire impact waveform was captured in one timeframe. INV9822 was the piezoresistive accelerometer, coated at the blade tip position. In general, accelerometers work on a principle of the inertia force of the mass acting upon an actual spring element, the acceleration of which is measured using strain gauges made of semiconductor material, and the device requires a low voltage supply. INV9822 has a diameter of 30 mm, and height of 50 mm, and the additional technical specifications are presented in Table 3.

Tab. 3. Types and technical specifications of the accelerometer

	Type	INV 9822
	Charge sensitivity, (mV/g)	100
	Weight, (g)	50
	Resolution ratio, (m/s^2)	0.0005
	Frequency response, (Hz)	0.5–8.0 k
	Resp. freq., (Hz)	> 25 k
	Impedance, (Ω)	< 100

TEST CONTROL STRATEGIES

A more sensitive measuring system is better to acquire the signal. However, in certain cases, the results may be unsatisfactory, resulting in the vibration levels at certain frequencies being excessively high or low. Note that an experiment is affected not only by the properties of the equipment, but also by the measurement system itself. The features must be considered in terms of the aliasing, leakage, windowing, filtering, zooming, and averaging. The accuracy of the measurements can be controlled to a large extent by the time spent in analysis, and this aspect must be considered during testing. For instance, a pre-trigger should be set correctly to ensure that the impulse on the points is captured immediately before the trigger is activated. A nearly perfect measuring system must be used when the charge amplifiers match well with the accelerometers and recording/displaying instruments.

In this work, the electrical devices were connected in series. The essential characteristic for the charge amplifiers (7021) is that they must have an extremely high input impedance. The dynamic signal analyser can automatically read the DOF and apply to the numbers with the correct directions. A charge amplifier was used at low frequencies, and the overall gain or sensitivity was thus independent of the transducer cable. Type 7021 and INV9822 require a low voltage power supply to be fed to the transducer; however, notable advantages can be attained in terms of a lower sensitivity to cable noise and fragility.

The data were supplied in analogue form; however, the digital instrument enabled signal processing through the analogue-to-digital conversion. The closed-loop system involved a four-channel digital signal processor, 306DF, which supported automatic active channel detection for the one-man calibration functionality. In general, the processor is a stand-alone unit with a frequency of 0–20 kHz. Because the system was assumed to behave in a linear manner, the FRF was composed of the sums of the resonance curves for each vibration mode. The processor could process the quantities in the form of a string of discrete values. Modal analysis transfers were intuitive to perceive. The common frequency response function analyser could be implemented through a tuneable narrow-band filter. Three impact events were performed at a point to perform averaging; nevertheless, the process was rapid.

The analysis software included a pre-process tool to assign the geometry data to points on the structure. The software could be configured with various levels of memory, displays, and data storage, and the measurement system was ensured to have sufficient channels to simultaneously record all the responses. The propeller resonances could be determined in this manner.

MEASUREMENT AND RESULTS

The aforementioned experiment strategy was used to obtain the natural frequency of the propeller in air and water. The presence of turbulence was ignored. The modal parameter estimation was based on the assumptions that the system was linear and stationary. The following steps were performed to configure the measurement system.

FREQUENCY RESPONSE MEASUREMENTS IN AIR

An accelerometer was placed at a certain position to capture the responses, specifically, point no. 45 at the tip of the blade. The accelerometer was attached with a stud adhesive. A total of 77 excitation points were selected from the scratched points on the propeller surface (shown in Fig. 5). These points were also input into the DASP.

For the vibration experiment in air, the entire process was performed at room temperature, as shown in Fig. 6. Note that it is difficult to fix the structure to the ground in real life. As shown in Fig. 6, this problem was overcome by physically fixing the hub between a steady disc and steel platform. In this manner, the displacements and rotations were set to nearly zero.

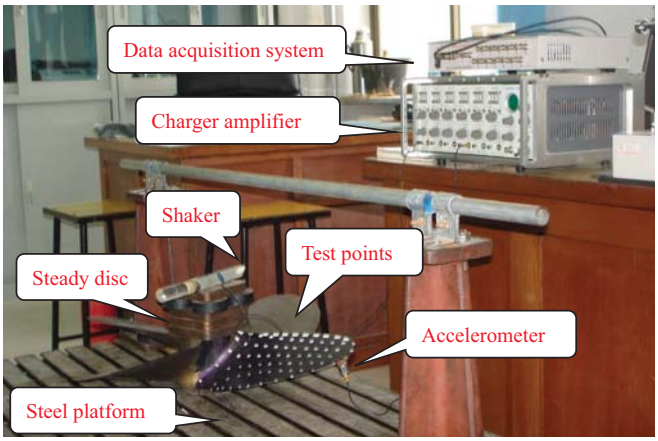

Fig. 6. Propeller 'hammer impact' vibration experiment under laboratory condition

Various modes of oscillation were captured simultaneously. Fig. 7 illustrates the experimental frequency: the measured response amplitude values were plotted as the solid curves, and the natural frequencies were determined using the scattered scanning research, indicated by the dashed lines. The geometry input allowed the generation of the wireframe. Typically, the model is created such that all points on the model correspond to the structure. Full 3D visualisation of the test is shown in Fig. 11.

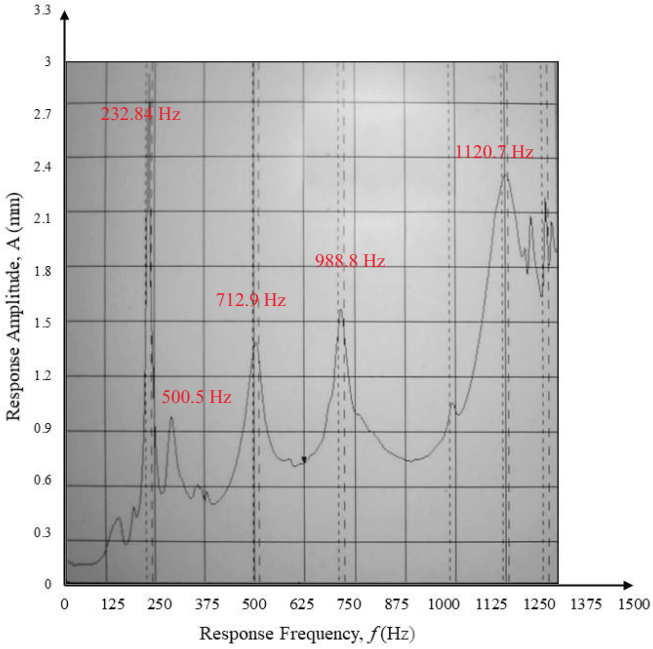

Fig. 7. Magnitude of the propeller response of the natural frequencies in air

FREQUENCY RESPONSE MEASUREMENTS IN WATER

The experiments in water were performed, as shown in Fig. 8, in a water body with sufficient dimensions. The hammer could not be used to realise point-by-point excitation, as in air. Single-point excitation and single-point response were recorded. Triggering was implemented for the analyser to start capturing data until an event occurred, such as the impact of the impact hammer. The mode shape in water was assumed to be identical to that in air. The sensor signals were protected against electromagnetic interferences by connecting the signal amplifier through shielded cables.

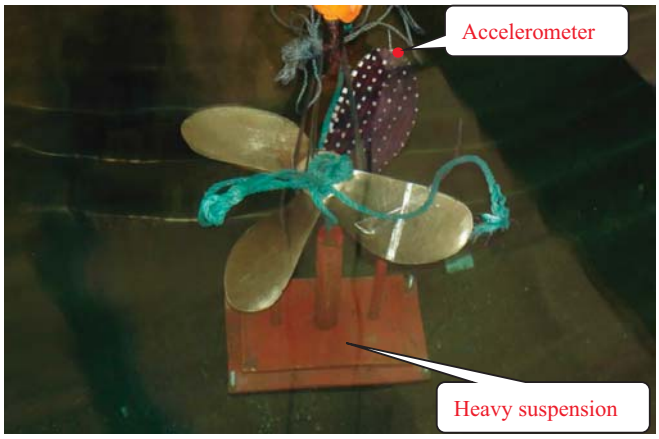

Fig. 8. Single-point excitation and single-point response experiment in water

In water, the structure was suspended and thus could not be regarded as being fully rigid. Nevertheless, as shown in Fig. 8, we could realise a sufficiently heavy suspension to approximate the necessary grounded condition.

The natural frequencies obtained through the DASP are shown in Fig. 9.

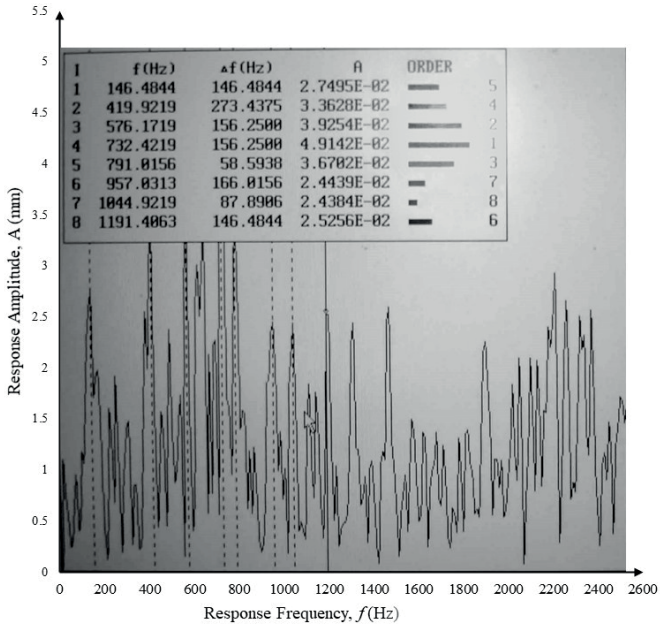

Fig. 9. Magnitude of the propeller response of the natural frequencies in water

The natural frequency of the FSI is lower than that in air, and the vibration of the blade is transmitted to the water, which increases the mass of water due to the dynamic behaviour. λ (%) in Eq. (5) reflects the frequency reduction

due to the FSI. Moreover, λ is often used to represent the FSI added water mass.

$$\lambda\,(\%) = 1 - \frac{f_{water}}{f_{air}} \tag{22}$$

After obtaining the signals of the dynamic characteristics in air and fluid, the vibration frequency was tabulated as in Table 4.

Tab. 4. Natural frequency of the tested propeller blade in air and water

Modes, n	Freq. in air (Hz)	Freq. in still water (Hz)	Reduction ratio λ%
1: 1st whipping	232.03	146.48	36.87%
2: 2nd whipping	500.49	419.92	16.10%
3: 1st torsional	712.89	576.12	19.19%
4: 1st flexural	988.79	732.42	25.93%
5: 2nd torsional	1120.6	957.8	14.53%

As demonstrated by the experiments of the propeller blades, the influence of the mass on the eigenvalues is dominant when the frequencies of free oscillations and those of their fields are reasonably close (the reduction does not exceed 40% but is no less than 25%). It was observed that the fluid notably influenced the reduction coefficients. When the resonance frequency of the system increased, the mass of water around the blade probably decreased. It is thus reasonable that the propeller is considered to be stationary. When the propeller rotates at a low speed, the frequency is not considered to be notably influenced [23].

VALIDATION AND DISCUSSION

Although coupled simulations can attain reasonable levels of accuracy and reliability for industrial and academic purposes, for the sake of robustness, the multi-physics algorithms offered by general-purpose codes are often adopted considering the coupling strategies presented earlier. Nevertheless, the code user must perform a practical validation to validate the coupling procedures. The validation generally requires a dedicated code to be developed, which may be extremely expensive. Therefore, in this work, the numerical validation was performed using ANSYS® through the APDL, and the existing element format was configured to add the user-defined parameters. The advantages of this aspect are obvious: low cost and high accuracy, high universality, and convenient analysis.

The propeller blades were considered to be a set of symmetrical blades, with the thickness changes taken into account. The blade root was thick, with the maximum thickness at the middle of the blade neck. The thickness decreased from the root of the blade to the tip. Fig. 10 illustrates the built FEM model and the real one, which are nearly identical. SOLID 185 elements were employed to discretise the propeller. The material had a density of 8.6×10^3 kg/m^3, Young's modulus of 120.0 GPa, and Poisson's ratio of 0.34.

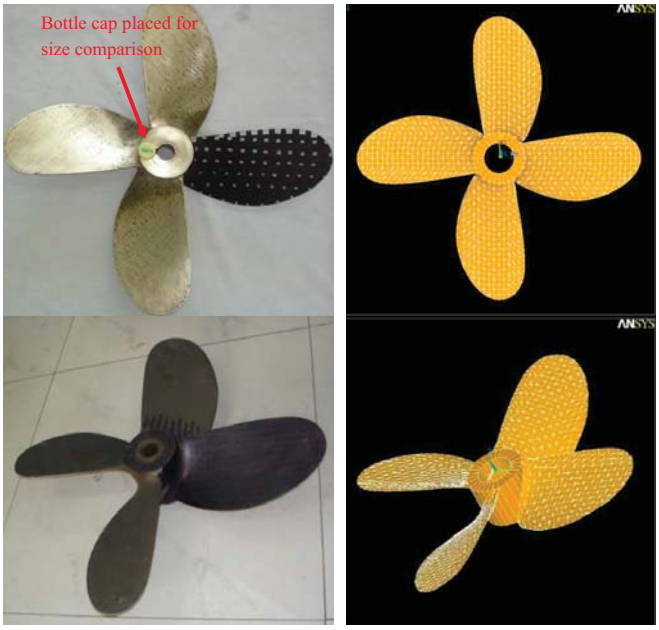

Fig. 10. Propeller structure and FEM model

The frequency obtained through the 4-blade isotropic structural computation was compared with that obtained considering the FSI of a single blade. The finite element model of a single blade was considered and assumed to fully emerge into the air medium. The speed of sound in air was defined to be 313.3 m/s, and ρ_o, which denotes the air density, was set as 1.29 kg/m^3. FLUID30 acoustic body elements in ANSYS® were used to simulate the air around the propeller. The governing equations for acoustics have been provided in Section 2. The FSI can be mapped automatically if the acoustic elements are adjacent to the solid structural elements. When using the coupled FLUID30, the displacement degrees of freedom were set as KEYOPT(2) = 0 on the interface to avoid zero-pivot warnings. It was necessary to define all the nodes on the interfaces. Thus, except for the nodes that lie on the interface and move with the structure, all the other nodes were established in space. The acoustic element on the interface was shared with the velocities or accelerations to realise direct coupling. The coupling matrices were discretised taking into account the acoustic pressure and structural displacement at the interface. We have tested that this arrangement of elements is sufficient for the observation of the global modal shapes, and fine division has been considered along the leading and trailing edges.

The effects of fluid around the propeller and structure itself were clarified, and the variables could be solved in a single time step by using the PCG Lanczos method in ANSYS®. The natural frequency results are presented in Table 5. The frequencies of the full model (not considering the FSI) were λ_1 = 234.87 Hz and λ_2 = 682.6 Hz. The solution of the model determined the free vibration of the propeller blade, taking into account their interaction and the influence of the

surrounding fluid: λ_1 = 232.67 Hz, and λ_2 = 686.12 Hz. The shape of the propeller oscillations in air was similar to that obtained through the structure simulation. The comparison in the last column clearly demonstrates a high agreement (see column 4 vs. column 6).

Tab. 5. Comparisons of propeller blade natural frequency between structural FE, FSI FE, and experimental results.

Modes, n	Experimental, *f*/Hz	Full model vibration, *f* (Hz)	Diff. %	Quarter model in air FSI, *f* (Hz)	Diff. %
1: 1st whipping	232.03	234.87	1.21%	232.67	0.28%
2: 2nd whipping	500.49	682.61	26.68%	686.12	27.06%
3: 1st torsional	712.89	756.79	5.80%	777.57	8.32%
4: 1st flexural	988.79	1275.57	22.48%	1248.38	20.79%
5: 2nd torsional	1120.6	1385.87	19.14%	1460.39	23.27%

The preceding mode shapes of the first five frequencies are illustrated in Fig. 11. The computation accuracy of the natural frequency of the FSI single blade exhibited the accuracy of the coupling analysis.

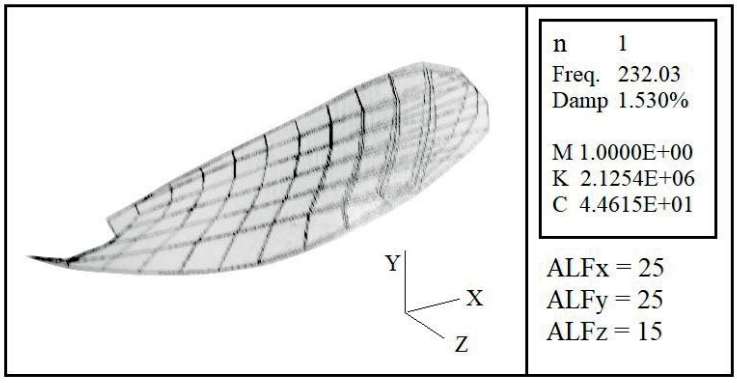

(a).1 experimental mode shape of f_1 = 232.03 Hz

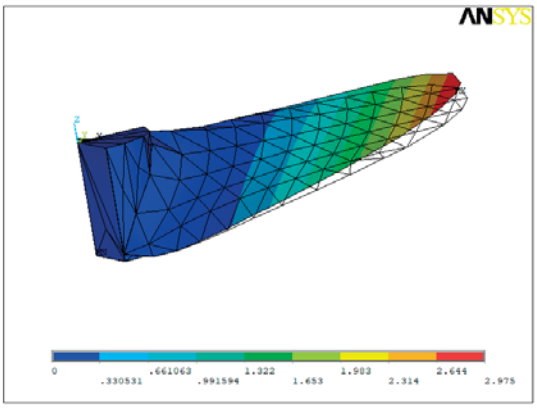

(a).2 numerical result of f_1 = 232.67 Hz

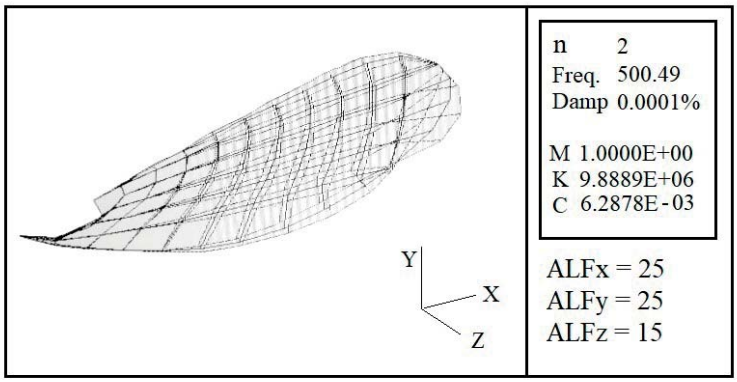

(b).1 experimental mode shape of f_2 = 500.49 Hz

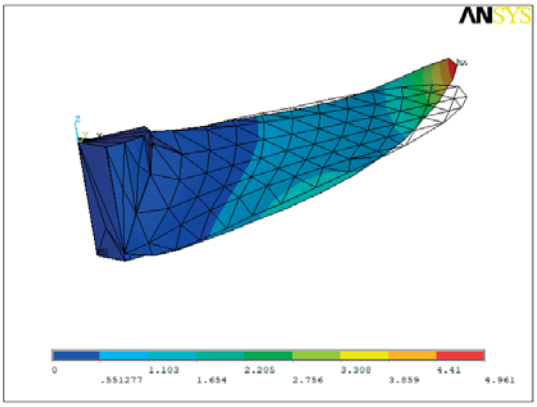

(b).2 numerical result of f_2 = 686.12 Hz

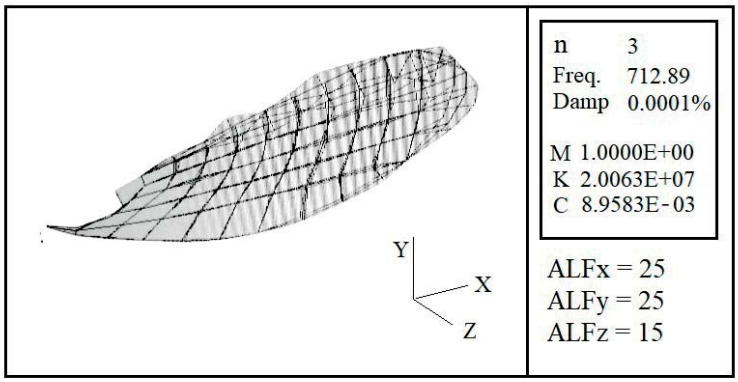

(c).1 experimental mode shape of f_3 = 712.89 Hz

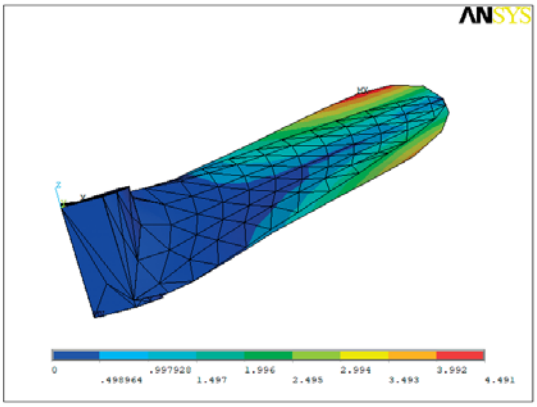

(c).2 numerical result of f_3 = 777.57 Hz

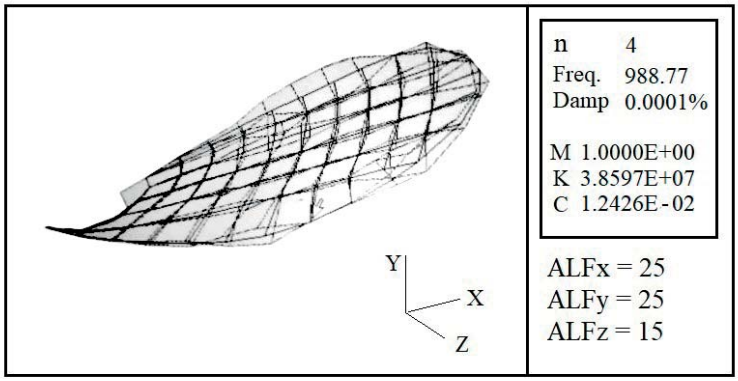

(d).1 experimental mode shape of f_4 = 988.77 Hz

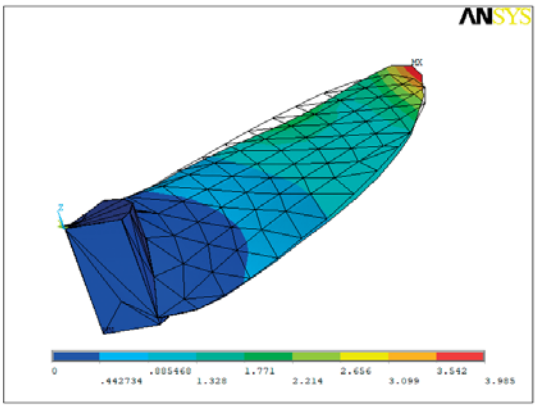

(d).2 numerical result of f_4 = 1248.38 Hz

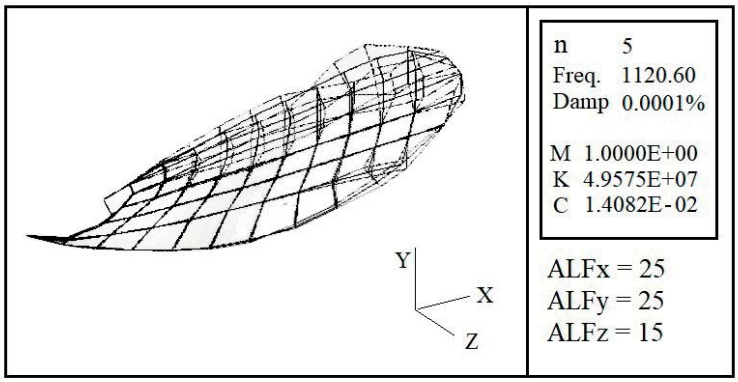

(e).1 experimental mode shape of f_5 = 1120.6 Hz

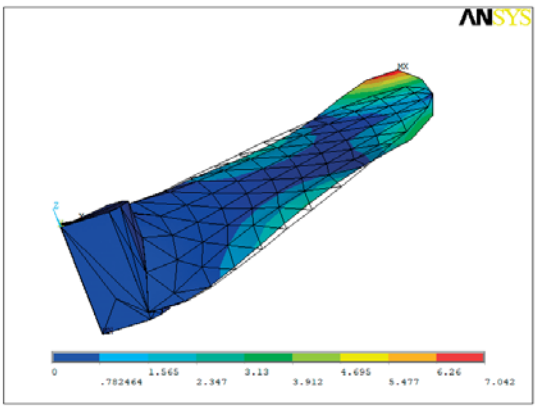

(e).2 numerical result of f_5 = 1460.39 Hz

Fig. 11. First five natural frequencies in air and their mode shapes: (a-e).1 show the experimental results, and (a-e).2 results obtained using ANSYS®

When comparing the results, considering the computation cost, error, accuracy and research priority, the single blade propeller could be applied for the water FSI FEM verifications. The fluid density of the water acoustic element was 1.03×10^3 kg/m^3, and the sound velocity c_0 in water was 1500 m/s. The vibration response analyses were limited to relatively large medium variations, and thus the changes in the harmonic response were large.

Under the assumptions that were validated numerically, the mode shapes were noted to be the same in air and water. For the convenience of comparison, the numerical results of the natural frequency in water and relative differences between these values with those obtained in the experiments are presented in Table 6. The added mass is recognised as an exclusive function of the body geometry, and its coefficient is incomparably affecting the reduction of the vibration natural frequency. The added masses effects (λ_i) of the FSI are presented in Table 7. Both these data points are illustrated in Fig. 12. The numerical modal analysis helped to identify the problem and generated an effective solution.

Tab. 6. Coupling frequencies of the numerical analyses and experiments in water

Modes, n	Numerical, *f*/Hz	Experimental, *f*/Hz	Differences, %
1: 1st whipping	143.63	146.48	1.95%
2: 2nd whipping	496.15	419.92	-18.15%
3: 1st torsional	567.44	576.12	1.51%
4: 1st flexural	1021.19	732.42	-39.43%
5: 2nd torsional	1141.09	957.8	-19.14%

Tab. 7. Results of the added mass related reduction factors and their absolute errors

Modes, n	Numerical λ, %	Experimental λ, %	Absolute errors, %
1: 1st whipping	38.27%	36.87%	1.40%
2: 2nd whipping	27.69%	16.10%	11.59%
3: 1st torsional	27.02%	19.19%	7.83%
4: 1st flexural	18.20%	25.93%	7.73%
5: 2nd torsional	21.86%	14.53%	7.33%

When the excitation force is known to coincide with one of the natural frequencies found in the modal analysis, the structure can be redesigned or modified to shift the natural frequency away from the excitation frequency. The explanation is analogous to that which explains the changes in the oscillation frequencies of the blades, when taking into account their interaction.

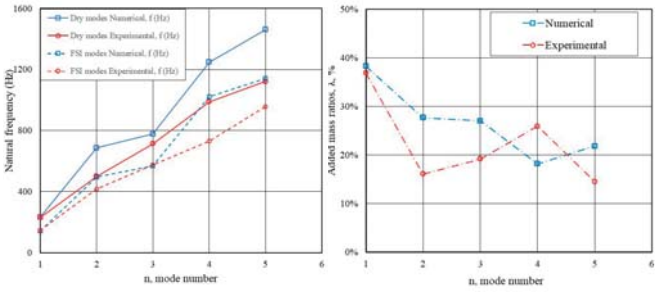

(a) (b)

Fig. 12 (a) Natural frequencies and (b) relative frequency reduction factor obtained using numerical calculations and experimental approaches.

After simplification, λ_1 was 38.0%, which satisfied the engineering practice values and approximately matched the conclusion presented by Carlton [1]. Some empirical formulas in inch units for the fundamental vibration natural frequency of propeller blades in air have been proposed by Carlton [1] and MacPherson et al. [30]. Modifying the formulas to international SI units, and considering our modal analysis in the experiment and FEM computation, the first-order natural frequency in water can be summarised using Eq. (23), in units of kg-mm-Hz.

$$f_{water} = \frac{0.0676}{(R - r_h)^2} \sqrt{\left(\frac{g \cdot E}{\rho}\right) \cdot \left(\frac{\bar{t}}{\bar{c}}\right) \cdot c_h \cdot t_h} \qquad (23)$$

where R is the propeller diameter, r_h is the blade root diameter, g is the acceleration due to gravity, E is the modulus of elasticity, ρ is the material density, $\bar{t}$ is the average thickness of the blade, $\bar{c}$ is the average chord length of the blade, t_h is the blade root thickness, and c_h is the chord length of the blade root..

CONCLUSIONS

In this paper, a modal experiment and coupling FEM were combined to analyse the vibration characteristics of a real propeller in air and water, to identify the vibration mode, and to obtain the natural frequency of the structure. After comparative and error analyses, the following conclusions could be derived.

1) The trends obtained using the existing numerical technology and experimental equipment were consistent. By comparing the results, it was confirmed that the direct coupling method employed could be used to realise the numerical computation of the vibration of complex underwater structures. Using the existing finite element tool, the results obtained exhibited not only high accuracy, but low resource consumption.

2) When the propeller vibrates at a low frequency in water, the influence of the surrounding fluid on the frequency of the propeller cannot be ignored. According to the results, the relevant data were retained, and an approximation was summarised in Eq. (23). The approximation has the advantage of being simple to use and does not require extensive computational resources and facilities.

3) The mode with the most obvious frequency reduction and the largest added water mass is the first-order mode. Most of the added water is generated by low frequency excitation. With the increase in the frequency and decrease in the excitation energy, the added water mass also decreases, resulting in the decrease in λ (in other words, less water mass will be coupled with the structure vibration).

4) Limited by the experimental conditions, errors were introduced during the experimental process: (1) the experimental constraint conditions were not entirely consistent with those in the FEM simulation. Especially for the test in water, a base or foundation on which the test structure can be attached is challenging. (2) The contact frequency between the knocking hammer and blade surface may cause the fluctuation of the power spectrum. (3) An accelerometer placed at the tip of the blade may change the mass distribution, which notably affects the 2nd whipping vibration shapes. All these aspects can affect the accurate recording of the test frequency. However, FEM simulations can overcome these physical limitations.

In addition, we demonstrated that the propeller design depends not only on the development of technology, but also on the feasibility of the engineering application. After comparing the numerical calculations and experimental results, the estimation requirements were noted to be satisfied; these findings are practical and can provide reference for the

propeller design. These data may help engineers design new structures without using advanced computing devices to determine the fundamental frequency λ_1 promptly.

REFERENCES

1. J. Carlton, "Marine propellers and propulsion, 2nd ed.," Butterworth-Heinemann, Oxford, 2012.

2. P. Król, "Hydrodynamic State of Art Review: Rotor–Stator Marine Propulsor Systems Design," Polish Marit. Res. 28 (1) (2021), 72–82. https://doi.org/10.2478/pomr-2021-0007

3. L.C. Burrill, "Marine propeller blade vibrations: full scale tests," Trans. NECIES, 1946, 62.

4. L.C. Burrill and W. Robson, "Virtual mass and moment of inertia of propellers," Trans. NECIES, 1962, 78.

5. M.G. Parsons, W.S. Vorus, and E.M. Richard, "Added mass and damping of vibrating propellers," Technical Report, University of Michigan, 1980.

6. S. Hyloarides and W. Van Gent, "Hydrodynamic reactions to propeller vibrations," in: Schip en Werf, 1979, 46.

7. H. Shen, D. Zhao, and Z. Luo, "Solution to eigenvalues of fluid-solid coupling vibration problem," J. Dalian Univ. Technol. 30 (3) (1990), 369–371. (In Chinese)

8. Z. Zheng, D. Zhao, and G. Wang, "Fluid-structure coupling kinetic analysis of propellers," J. Dalian Univ. Technol., 36 (1996), 199–223. (In Chinese)

9. J. Xiong, D. Zhao, and J. Ma, "Dynamic analysis of propeller blades," J. Dalian Univ. Technol. 40 (2000), 737–740. (In Chinese)

10. A. Korotkin, "Added masses of ship structures (Vol. 88)," Springer Science & Business Media, 2008.

11. H. Ghassemi and E. Yari, "The added mass coefficient computation of sphere, ellipsoid and marine propellers using boundary element method," Polish Marit. Res. 18 (2011), 17–26. https://doi.org/10.2478/v10012-011-0003-1

12. P. Castellini and C. Santolini, "Vibration measurements on blades of a naval propeller rotating in water with tracking laser vibrometer," Measurement 24 (1998), 43–54. https://doi.org/10.1016/S0263-2241(98)00044-X

13. [13] S.H. Abbas, J.K. Jang, D.H. Kim, and J.R. Lee, "Underwater vibration analysis method for rotating propeller blades using laser Doppler vibrometer," Opt. Laser Eng. 132 (2020), 106133. https://doi.org/10.1016/j.optlaseng.2020.106133

14. L. Guangnian, Q. Chen, and Y. Liu, "Experimental study on dynamic structure of propeller tip vortex," Polish Marit. Res. 27 (2) (2020), 11–18. https://doi.org/10.2478/pomr-2020-0022

15. G. Vaz, D. Hally, T. Huuva, N. Bulten, P. Muller, P. Becchi, J.L. Herrer, S. Whitworth, R. Macé, and A. Korsström, "Cavitating flow calculations for the E779A propeller in open water and behind conditions: code comparison and solution validation," in Proceedings of the Fourth International Symposium on Marine Propulsors (SMP) 15 (2015), 344–360.

16. H. Nouroozi and H. Zeraatgar, "Propeller hydrodynamic characteristics in oblique flow by unsteady RANSE solver," Polish Marit. Res. 27 (1) (2020), 6–17. https://doi.org/10.2478/pomr-2020-0001

17. A. Nadery and H. Ghassemi, "Numerical investigation of the hydrodynamic performance of the propeller behind the ship with and without Wed," Polish Marit. Res. 27 (4) (2020), 50–59. https://doi.org/10.2478/pomr-2020-0065

18. Y. Zhang, X.P. Wu, M.Y. Lai, G.P. Zhou, and J. Zhang, "Feasibility study of RANS in predicting propeller cavitation in behind-hull conditions," Polish Marit. Res. 27 (4) (2020), 26–35. https://doi.org/10.2478/pomr-2020-0063

19. J.F. Sigrist, "Fluid-structure interaction: an introduction to finite element coupling," John Wiley & Sons, West Sussex, United Kingdom, 2015.

20. Z. Suo and R. Guo, "Hydroelasticity of rotating bodies—theory and application," Marine Struct. 9 (1996), 631–646. https://doi.org/10.1016/0951-8339(95)00010-0

21. H. Lin and J. Lin, "Nonlinear hydroelastic behavior of propellers using a finite element method and lifting surface theory," J. Mar. Sci. Technol. 1 (1996), 114. https://doi.org/10.1007/BF02391167

22. D. Zou, J. Zhang, N. Ta, Z. Rao, "The hydroelastic analysis of marine propellers with consideration of the effect of the shaft," Ocean Eng. 131 (2017), 95–106. https://doi.org/10.1016/j.oceaneng.2016.12.032

23. J. Li, Y. Qu, H. Hua, "Hydroelastic analysis of underwater rotating elastic marine propellers by using a coupled BEM-FEM algorithm," Ocean Eng. 146 (2017), 178–191. https://doi.org/10.1016/j.ocean eng.2017.09.028

24. Y. Young, "Time-dependent hydroelastic analysis of cavitating propulsors," J. Fluid. Struct. 23 (2007), 269–295. http://dx.doi.org/10.1016/j.jfluidstructs.2006.09.003.

25. Y. Young, "Fluid-structure interaction analysis of flexible composite marine propellers," J. Fluid.

Struct. 24 (2008), 799–818. http://dx.doi.org/10.1016/j.jfluidstructs.2007.12.010.

26. X. He, Y. Hong, and R. Wang, "Hydroelastic optimisation of a composite marine propeller in a non-uniform wake," Ocean Eng. 39 (2012), 14–23, http://dx.doi.org/10.1016/j.oceaneng.2011.10.007.

27. H. Lee, M.C. Song, J.C. Suh, B.J. Chang, "Hydro-elastic analysis of marine propellers based on a BEM-FEM coupled FSI algorithm," Int. J. Nav. Archit. Ocean Eng. 6 (2014), 562–577. http://dx.doi.org/10.2478/IJNAOE-2013-0198.

28. J. Neugebauer, M. Abdel-Maksoud, and M. Braun, "Fluid-structure interaction of propellers," in IUTAM Symposium on Fluid-Structure Interaction in Ocean Engineering 2008, (pp. 191–204). Springer, Dordrecht.

29. S. Kapuria and H. Das, "Improving hydrodynamic efficiency of composite marine propellers in off-design conditions using shape memory alloy composite actuators," Ocean Eng. 168 (2018), 185–203. https://doi.org/10.1016/j.oceaneng.2018.09.001

30. D.M. MacPherson, V.R. Puleo, and M.B. Packard, "Estimation of entrained water added mass properties for vibration analysis," SNAME New England Section, 2007.

31. J. Xing, "Natural vibration of two-dimensional slender structure–water interaction systems subject to Sommerfeld radiation condition," J. Sound Vib. 308 (2007), 67–79. https://doi.org/10.1016/j.jsv.2007.07.009

32. O.C. Zienkiewicz and R.L. Taylor, "The finite element method: solid mechanics," Butterworth-Heinemann, Oxford, 2000.

33. X.C. Wang, "Finite element method," Tsinghua University Press, 2002. (In Chinese)

34. E. Kock and L. Olson, "Fluid-structure interaction analysis by finite element method: a variational approach," Int. J. Num. Mech. Eng. 31 (1991), 463–491. https://doi.org/10.1002/nme.1620310305

CONTACT WITH THE AUTHORS

Hongyu Cui
e-mail: cuihongyu@dlut.edu.cn

Dalian University of Technology, Linggong Road,
Number 2,
Ganjingzi District, 116081,Dalian
China

Benqiang Lou
e-mail: benqiang.lou@hotmail.com

Jiangsu University of Science and Technology,
Changhui Road, Number 666,
Changhui Road, 212003 Zhenjiang
China